OBSERVATION OF IR SOURCE AT OCEAN HORIZON[1]

E. H. Takken, M. D. Mermelstein, E. J. Stone, and R. G. Priest
Naval Research Laboratory, Washington DC 20375

M. Kaelberer and D. Crowder
Naval Surface Warfare Center, Silver Spring MD 20903

Steven R. Church
Areté Associates, Sherman Oaks CA 91413

D. P. Brown and J. Fisher
Maryland Advanced Development Laboratory, Greenbelt MD 20770

ABSTRACT

Disappearance of a small electrically-heated infrared source over the ocean detection horizon was observed during a field test in June 1994 at Monterey Bay CA. The source was flown beneath a helicopter at low altitudes in a northwesterly direction from an imaging infrared sensor 29.5 m above sea level on a bluff at Fort Ord overlooking the Bay. The data reported here were taken out to ranges of 25.2 km. Radiometrically calibrated 256x256 digital images of 127 microradian resolution were acquired at 30 frames per second with an NEI of $\approx 3 \times 10^{-16}$ W/cm^2 in a narrow 3.75-4.11 μm spectral band. Visible-band land-to-land intervision tests of ocean surface occlusion were conducted concurrently along a path across the southern end of the Bay.

This report addresses five related issues of infrared phenomenology relating to IRST detection of cruise missiles over the ocean: (1) the observed contrast produced by the source as a function of range; (2) the observation of birds to ranges of ≈6 km in the imagery and a model for their detection in the MWIR; (3) the observed strong scintillation of the distant source over the ocean as compared to calculations of this phenomenon; (4) wave surface effects on viewing cutoff and consequences for marine boundary layer modeling; (5) horizon radiance profile modeling with comparison to the image data to fit mean ocean radiance and clutter. The validity and utility of Lowtran in modeling transmission phenomena for long low overwater paths is also discussed.

1.0 FIELD TEST EQUIPMENT AND SENSORS

A sketch of the Monterey Bay test site location is shown in Figure 1. The land-to-helicopter observations were made along northwestward paths out over the ocean from Fort Ord. The land-to-land test, on the other hand, was conducted with views across the bay between Marina and Point Pinos. Data reported here is for the days June 26 and June 30.

In the land-to-helicopter test a small hot infrared source was carried to positions and altitudes of choice out over the open water. Though more costly, the helicopter with laser altimeter proved far more reliable for operating in stiff winds at steady, known heights above the waves than the boats that have been used in the past. The main limitations of the tests came from the buoys and boats used to gather meteorology and oceanography. The buoy's equipment failed and could not be repaired within the time frame of the test, so all meteorological data had to be taken or extrapolated from that of the met boat during the times when it was able to operate. Land-to-land viewing across open water gives the best determination of heights and offers the possibility of operations under a much wider range of meteorological conditions. The land-to-land tests done during this field test, however, were a preliminary evaluation of the approach and used only marginally sufficient equipment.

---

[1]This work was sponsored by the Office of Naval Research. Support of Bill Morris, Doug Jensen, Travis Metcalf, Paul Frederickson, Doug McKinney, Ken Davidson, Mike Daley and Charles Gott is gratefully acknowledged.

1.1 Land-to-Helicopter Equipment

A four-seat commercial helicopter was fitted for this test series with a laser altimeter, GPS (Global Positioning System) transponder and a controlled infrared source. With the altimeter, instantaneous heights accurate to a few cm were recorded with clock time. As shown in Figure 2 for June 30, wave motion is clearly evident in the recordings. From expanded plots of laser altimeter data source height accuracy appears to be on the order of a meter. Differential GPS between units in the helicopter and the sensor base station gave an accuracy of 5 m in relative position . These ranges are also included in Figure 2.

Photographs of the helicopter in flight and of the electrically heated infrared source are shown in Figure 3. The distance from the center of the source to the hot exhaust of the helicopter engines was approximately 23.5 meters. These two were the only features apparent in the IR imagery at significant ranges. Electrical power to the IR source could be varied but was generally set at its full power of 868 watts.

The infrared source consisted of a cylindrical electric heater 3.3 cm in diameter and 13 cm in height that was enclosed and protected from wind by a nominally IR-transparent shroud 41 cm in diameter and 49 cm tall To determine effective temperature, emissivity and pass band of this heater as viewed through the shroud, a spectral radiance measurement was made of its surface at short range prior to the field test.

The infrared sensor used during these tests was an Amber mid-wave 256x256 InSb array with an F/3, 300 mm focal length lens with 6" clear aperture. This gives images with 127 μrad pixels. The optical blur of the lens is near diffraction limited which is about half the detector size. Focusing based on simple visual inspection of sensor screen display of the horizon scene turns out to be surprisingly accurate. Continuous recordings at 30 frames per second show that the amount of time spent straddling two pixels by a moving point source is relatively short, so the focusing blur really was set by image inspection to smaller than the detector size. This does not mean, however, that any significant amount of radiation was lost to non responsive areas between detectors. In the InSb array fabrication the non-responsive region between detectors is about 5% of their spacing. And in the data the summed response to a point source straddling two pixels is found to be the same as when it is in a single pixel.

Analog SVHS recording of the infrared imagery proved to have inadequate dynamic range. Digital recording was necessary. It was done in either of two ways -- either by capturing a single frame of data from the image display buffer and storing it on disk or by recording continuously on an Amber DCRSi tape recorder. The formats for these VRAM and DCRSi files are a bit involved, but are essentially unsigned two-byte integers that are to a good approximation linearly proportional to the photon flux focused on the array by the optics. The gains and offsets of this linear relationship are manipulated to be the same for all detectors by the digital non-uniformity correction (NUC) electronics in the sensor. For the two-point calibrations special care had to be used when bracketing the scene with the high and low temperature blackbodies. The water off the coast of California is cold, so T_{high} and T_{low} were usually set colder or significantly colder than the temperature of the room with the sensor and lens.

The resulting single-frame VRAM radiance images have been stored as four-byte real pixels in HDF SDS format for easy loading and analysis with commercial software tools. Continuous-frame DCRSi imagery, though, has been stored as one-byte unsigned integer pixels in raster HDF format and for these a separate note must be kept of the relationship between the one-byte pixel values and radiance. This data will be made available on various media through QuesTech[2] as part of the IRAMMP program. In the meantime a subset of the data can be retrieved via anonymous FTP. A sampling of fifteen June 30 images of the helicopter and source just above the horizon is given in Figure 4.

The limiting noise in this staring array was a slight beat-frequency interference that cast itself as a dominating checkerboard pattern in individual scenes. The electronics contains four A/D channels arranged to read a raster of 2x2 super-pixels across the array. The interference was strongest in one of the four A/D channels so that a periodic fluctuation tended to occur in one corner of the 2x2 super-pixel scan across the image. This creates a local checkerboard pattern in the full 256x256 image but a furrow-like variation in intensity in a single-channel 128x128 subimage. This furrow effect changes from scene to scene and is somewhat variable within a given subimage with a frequency from 15 to 25 cycles per image width. Still, the noise performance of the sensor with the cool 9-19 °C calibration on June 30 was quite good:

---

[2]Point of contact at QuesTech is Mike Eggleston, 703-760-1133.

$$NEI_{3.75\text{-}4.11\,\mu m} \approx \begin{cases} 3 \text{ to } 6 \times 10^{-16}\ W/cm^2; & \text{June 30} \\ 1 \times 10^{-15}\ W/cm^2; & \text{June 26} \end{cases} \quad (2)$$

The better NEI can be achieved by specialized channel filtering to remove some of the mentioned sensor artifacts.

1.2 Land-to-Land Equipment

The land-to-land tests were an exploratory evaluation of how to conduct detailed studies of wave limiting on viewing across the ocean surface. It is much easier to work in the visible than the infrared, and both experience essentially the same ray bending because the index of refraction is very nearly the same in the two bands. A literature survey of the index of refraction of air has been given by Dion et. al., [3,4,5,6] and their expression suggests about a 2 % difference. So a simple flash lamp was used as a source and viewed through binoculars over a known path length. The source would be placed at a convenient known height relative to the tide, and the person with the binoculars would move downward along the beach to precisely known heights and count flashes to determine the probability of ray-path cutoff by the waves.

The use of a visible band flash lamp with low daytime contrast tended to limit these land-to-land tests to night time operations. This conflicted with the schedule of the meteorology boat that often declined to go out at after dark.

Precise surveying, tide and wave-height measurements are the cornerstones for accurate wave-limit tests of cross-ocean viewing. The site survey was conducted using GPS averaging instrumentation with a height accuracy of ±5 cm. Tides were measured by NOAA. Wave height should be measured with buoy instrumentation, but all that was available during these tests was a boat captain's visual estimate.

1.3 Meteorology

Here the term "meteorological parameters" is meant to include both atmosphere and ocean surface data, that is, water temperature, wave height and tide data along with low-altitude air temperature, humidity, wind velocity, C_n^2, visibility, aerosol character and radon count. Except for the tide information from NOAA most of the available "met" data was taken from a 35' boat. The values recorded were air temperature and humidity 2.7 m above the surface, wind speed and direction at 3.1 m, surface temperature and clock time. C_n^2 measurement was not available due to equipment failure. Wave height was estimated visually. Availability of this data was limited by the seaworthiness of the boat, and for the land-to-land tests it is was sometimes necessary to extrapolate by an hour or two from the last measurements the boat was able to make before returning to port. Visibility over the ocean was available from the local airport. Aerosols and air temperature at higher altitudes were measured by the NOSC met aircraft, and radon count was measured at the sensor test site.

2.0 LOWTRAN AS A MODELING TOOL IN COASTAL ENVIRONMENTS

The use of Lowtran as a modeling tool for the geometry and atmospherics of interest to the Navy can be problematic. Having the correct and complete field data for inputs over the optical path is more of an issue than the inherent validity of the code. And the variability of meteorological conditions along a 20-30 km viewing path can be particularly troublesome close to shore. The calculation of radiance is more uncertain than that of transmission.

Default atmospheres can not be used. The temperature, pressure and constituents of the atmosphere have to be modeled as layers, and the low-elevation thicknesses of these layers need to be thin for near-horizon viewing

---

[3] D. Dion, B. Leclerc and C. Lassonde, "Investigation of the Air Refractivity Effects on IR Sensors in the Marine Boundary Layer, Eqs. 2.3-2.10, Dossier 3632C-037, DREV, Valcartier, Canada, 418-844-4231, March 1989.

[4] B Edlén, "The Dispersion of Standard Air," J. Opt. Soc. Am., Vol. 43, No. 5, pp. 339-343, May 1953.

[5] R.H. Hill and R.S. Lawrence, "Refractive-index and Absorption Fluctuations in the Infrared Caused by Temperature, Humidity and Pressure Fluctuations," J. Opt. Soc. Am., Vol. 7-, No. 10, pp. 1192-1205, Oct. 1980.

[6] R.J. Hill and R.S. Lawrence, "Refractive Index of Water Vapor in Infrared Windows," Infrared Phys., Vol. 26, No 6, pp. 271-376, Great Britain, 1986.

paths. What is used for fitting the data of this field test is a temperature-humidity modification of the US. Standard Atmosphere. Below an altitude of 100 m temperatures have been scaled so that they match the boat-measured air temperature at 2.7 m altitude. At the lower altitudes the temperature distribution was made to fit a marine atmospheric boundary model distribution, and layer thicknesses were exponentially spaced near the surface. Relative humidity was similarly scaled except that it can not be set too high near the surface. Lowtran adjusts aerosol size with relative humidity, and this increases rapidly as humidity exceeds 95 % so as to unduly degrade transmission along calculated paths. So in the calculations reported here humidity has usually been fixed at 75 %.

Ray bending in the dispersive atmosphere is tracked by Lowtran, and this requires better than single precision calculations. Either Modtran has to be used or a recompiled version of Lowtran 7. The spectral resolution of Modtran is not needed, but the ray geometry part of this code has been cast as double precision.

Ocean aerosols tend to dominate infrared transmission losses in atmospheric windows such as the one at 4 μm used for the present field test. The marine aerosol model[7] contained in Lowtran for calculating transmission requires four input parameters which need to be carefully understood: relative humidity ≤ 98 %; land-aerosol mass parameter, ICSTL = 1 to 10; current wind speed $V_{present}$ and average wind speed V_{24hr}. Visibility is an optional "override" parameter that is best to omit for infrared calculations. The code contains three aerosol distributions which for 80% relative humidity have dN/dr peaks centered at 0.03 μm, 0.24 μm and 2.0 μm. The smaller particles represent non-marine aerosols, the peak of which is set by land-aerosol mass parameter. Depending on the data available one should use either ICSTL = int(RC/4) + 1, where RC is radon count in picocuries per m^3 or perhaps ICSTL = int[9exp(-TD/4)] + 1, where TD is the number of days the air has been blowing over the ocean. The larger aerosols arise from sea spray, and the peaks of their density distributions are set by the two wind speeds, the largest being more influenced by V_{24hr}. The aerosols are all assumed to be hygroscopic, so that they grow in size with relative humidity - as by a factor of two from 80 % to 95 % relative humidity. The size relationship used is not valid above 98 % relative humidity. If visibility is left null for an input it is calculated by the marine aerosol code. But if visibility is included in the inputs, the code first uses wind speeds (and ICSTL if available) to set both sea and land aerosol densities, and then adjusts the counts of all particle sizes up or down in unison so as achieve the asserted transmission at 0.55 μm. One needs to be careful to understand that this overrides the normal dependence of sea aerosol densities on wind speed.

During the field test reported here the meteorological conditions sometimes changed in times as short as the wind transit time down the sensor viewing path. This means both that aerosol distributions and air index of refraction profiles were probably not laterally uniform, so that input parameters for calculations using homogenous models are not well defined by the available point meteorological measurements. A particular problem is what to use for V_{24hr} when winds at the test sight undergo strong diurnal changes from sea-land to land-sea breeze. And even if the sea-land breeze were steady, the coastal met conditions would still be in question because the air would be passing a kilometer or so inland, rising and then returning from only several tens of kilometers over the water. So the inputs to the marine aerosol model in Lowtran were sometimes varied from point meteorological measurements in order to achieve a fit with the field test data presented later, and on occasion the visibility override was even used. Table 1 gives a sensitivity analysis of the marine aerosol model on its four input parameters. The black body dependence is implicit in user atmospheres.

Table 1: Radiance Sensitivity Analysis for Lowtran and Black Body

Condition	Visibility	ICSTL	V_{24hr}	$V_{present}$	Black Body
Nominal	17.8 km	9	4.0 m/s	1.0 m/s	285.7 °K
Δ Radiance per unit	1.6 %	-0.9 %	1.0 %	8.3 %	2.7 %

The marine aerosol model assumes that aerosol particle sizes are independent of height in the first kilometer. It does not include the large aerosols ≥10 μm in size that are known sometimes to increase below

[7] S.G. Gathman, *Optical Properties of the Marine Aerosol as Predicted by the Navy Aerosol Model*, Optical Engineering, Vol. 22, No. 1, p. 67, Jan/Feb 1983

30 m,[8,9,10,11] and certainly not the largest ≈ 200-300 μm in size expelled into the first 18 cm that fall back to the surface.[12] This is a valid approximation for calculations of infrared transmission, especially for the mid wave, because the low-layer particle density distribution drops off with size as $dN/dr \propto r^{-4.0}$ to $r^{-4.5}$. Thus their attenuation of infrared (0.6 times their integrated area $\int dr\{dN/dr\}r^2$) is negligible even though the integrated volume of these large particles $\int dr\{dN/dr\}r^3$ is finite and does contribute to upward mass transport and weather.

Now inherent in Lowtran-Modtran is a thermodynamic equilibrium assumption about re-emission scattering of radiation from aerosols along the viewing path. This has been left unchanged even though there is significant vertical asymmetry of temperatures along paths to the ocean horizon. The trend of calculated results is that when single and then multiple aerosol scattering are invoked, path radiance first increases and then decreases.

Lowtran is assumed to be a valid tool for calculating fits to the infrared data measured on this field test. The available meteorological data is limited in scope, and one has to use care is specifying the Lowtran inputs.

3.0 BIRDS

The easiest measurements to describe and to fit with modeling are those for birds. Large numbers of gulls and cormorants were observed flying through the field of view of the sensor, generally parallel to the shoreline and perpendicular to both the line of sight and the sea-land wind direction. Playback of the DCRSi recordings shows a significant number of them. Ranges are estimated from observed angular crossing rates to be as great as 6 km, based on an assumed speed of 9 m/sec. [13]

Though birds have not often been reported in the MWIR before, one could easily expect them to become common solar-illuminated sources of clutter for infrared detection and tracking systems. The transition from solar-dominated to thermal-dominated background clutter occurs near 3.8 μm. Target detection is done on the basis of contrast, and here the contrast is with respect to a largely thermal and very uniform background. The spatial-temporal noise level is low, on the order of 10^{-15} W/m^2/sr for this sensor on this day. Thus the reflected solar radiation is expected to be the more significant contributor to contrast.

To put this argument in quantitative terms, start with the solar irradiance received at the surface of the earth in the 3.75-4.11 μm band, which is $Q_{sun} = 2.5 \times 10^{-4}$ W/cm^2 (from Lowtran) but depends on time of day and atmospherics. We collected gull feathers and measured their diffuse reflectance in this waveband to be $\rho = 0.18$. Then if the effective surface area of a bird is $A_{bird} \approx 100$ cm^2 the reflected solar contribution to contrast radiant intensity is ~1.4×10^{-3} W/sr. The thermal contrast radiant intensity, using emissivity 0.82, and guessing temperature 1 to 10 C above ambient, is ~-1 to +4 x 10^{-4} W/sr, roughly an order of magnitude smaller.

The range at which a sunlit bird may be seen by a sensor with signal-to-noise ratio of 2 is estimated from

$$\rho\, Q_{sun}\, \tau_{atm}\, A_{bird}\, A_{sensor} / \pi R^2_{to\ bird} = A_{sensor}\, 2\, NEI$$

to be

$$R_{to\ bird} = \sqrt{\rho\, Q_{sun}\, \tau_{atm}\, A_{bird} / 2\pi\, NEI} \approx 6\ km \qquad (3)$$

---

[8] G. de Leeuw, *Vertical Distributions of Sea-Spray Particles at Low Heights and Calculated Extinction Coefficients*, Report No. FEL 1985-33, Physics and Electronics Laboratory, TNO, 2509 JG The Hague, The Netherlands, phone 31-70-26-42-21-32397, 1985.

[9] G. de Leeuw, *Mixed-Layer Profiling with Lidar and Modeling of the Aerosol Vertical Structure*, No. 14, pp. 100-104, Proceedings of the NATO Advanced Workshop on Humidity Exchange Over the Sea Main Experiment (HEXMAX) Analysis and Interpretation, Dellenhove, Epe, The Netherlands, April, 1988, ed. W.A. Oost, S.D. Smith and K.B. Katsaros.

[10] G. de Leeuw, *Surface Layer Profiling of Aerosol Concentrations, Particle Size Distributions and Relative Humidity*, No. 11, pp. 80-85, HEXMAX, 1988

[11] W.A. Oost, *HEXMAX Review*, No. 3, pp. 7-13, HEXMAX, 1988.

[12] D.C. Blanchard, *Electrification of the Atmosphere*, pp. 77-202 in Progress in Oceanography, Volume 1, ed. M. Sears, Pergamon Press, MacMillan Co., 1963.

[13] G.D. Schnell and J.J. Hellack, *Bird Flight Speeds in Nature: Optimized or a Compromise?*, American Naturalist, vol. 113, p. 53-66 (1979).

in good agreement with that obtained from crossing rates in the imagery.

4.0 RADIANCE OF IR SOURCE VS RANGE

A set of nearly 100 VRAM images similar to those of Figure 4 were recorded on June 30. The test lasted for an hour and a half, and as shown in Figure 2 the helicopter traveled out to 25.2 km. It could be tracked with the infrared sensor at this range but had disappeared to the naked eye at several kilometers. There was typically dense haze over the cold Pacific coastal waters with late afternoon forward scattering of the sun.

Plots of measured low-elevation background radiance and of target contrast radiance measured from this sequence of images are given in Figures 5 and 6, along with calculated values obtained using the Lowtran mode of Modtran. In calculating background (path radiance) in Figure 5, solar scattering was important, about 10 to 15% of the total, because of the strong forward scattering. The sun's position was incremented at 5 minute intervals, along with appropriate meteorological parameters. The solar contribution increased from 6:00 to 7:30 pm as the sun moved nearer to the viewing path but decreased thereafter because of the greater atmospheric attenuation from space. The measured and calculated values of background radiance are in fairly good agreement. Visibility and land-aerosol mass parameter are being treated as fitting parameters in Lowtran. Seeing conditions for the day were moderate.

Measured source contrast was found by comparing the target pixel radiance with an average of nearby background pixels. The source was modeled as an unresolved 727 K, 43 cm^2 greybody of emissivity 0.8. The variation in observed radiance is no doubt due to scintillation (see below) as well as spatio-temporal noise. The target measurements show contrast falling off much less rapidly than the prediction beyond 18 km range; this effect is not understood. Because of the strong source scintillation a selection effect may be involved: we measured only what we could see.

5.0 SCINTILLATION

A carefully selected sequence of 1155 images covering 38.5 seconds of infrared imagery was taken from the DCRSi recordings on June 26 when the range to the helicopter and IR source was 23.5 km. This sequence clearly shows scintillation and was chosen because it brackets about a 10 second period when the source was below the apparent horizon. This data of consecutive observed source intensities, acquired at 30 frames per second, is shown in Figure 7.

The helicopter was attempting to hold a fixed height during this sequence of images, but wind carried it slowly across the field of view and its altitude varied slightly. Both the source and helicopter apparent intensities scintillate strongly, but they do not blur across or dart between pixels. Then after some ten seconds the helicopter dropped by one pixel and the source disappeared. As can be seen in Figure 7, it was not just scintillating. It disappeared for an extended period and could only have dropped below the detection horizon. Then for the last 10-15 sec the helicopter rose one pixel up to its original elevation, and the scintillating source reappeared.

It is evident from this data that a sensor with a short look time, such as a scanning IRST, could easily miss the presence of a target at the horizon.

With J the measured source contrast in sensor counts, the mean and standard deviation of this scintillating source are

$$\langle J \rangle = 71.3 \text{ counts} \quad \text{and} \quad \sqrt{\langle (J - \langle J \rangle)^2 \rangle} = 34.0 \text{ counts, or } 48\% \tag{4}$$

The autocorrelation function for these fluctuations indicates a correlation time of approximately the integration time of the sensor. In other words, the scintillation is uncorrelated at this sampling rate, and the variability of the actual scintillation must be faster than 1/30 sec.

Met data at the time of this scintillation measurement were $T_{surface}$ = 10.0 C, T_{air} = 10.7 C, V_{wind} = 1.6 m/sec, and relative humidity = 96%. This air-sea temperature difference (ASTD) of + 0.7 C can produce turbulence which causes scintillation. However, the met boat recorded data every ten minutes, and the previous value for air-sea temperature difference was + 0.4 C, a significantly smaller value for driving turbulence. Calculations have been done using both values.

To perform modeling calculations for scintillation and correlation time one needs two classes of input parameters - meteorology and geometry. Met conditions at the time of this scintillation measurement are summarized in Table 2. The strong positive air-sea temperature difference (ASTD) does imply significant scintillation, but conditions were undergoing rapid change, and it is not clear exactly what parameters to use in modeling that assumes lateral uniformity. The met boat was located at the time of the measurement well on the leeward side of the horizon tangent region of the viewing path, so perhaps preference should be given to the earlier wind and temperature measurements.

TABLE 2 BOAT METEOROLOGICAL CONDITIONS ON JUNE 26

Time (am, PDT)	ASTD (°C)	V_{wind} (m/sec)	RH (%)	T_{air} (°C)	T_{water} (°C)
8:50	+0.4	1.8	96	10.5	10.1
9:00	+0.7	1.6	95	10.7	10.0
9:10	+0.9	1.3	96	11.1	10.2

Air Pressure = 1015.6 mB

As already noted there were no laser altimeter readings on this day, but source height can be estimated in several ways. The voice log of communication with the helicopter pilot indicate that the source height should be in the range of 2 to 15 meters. The source is in the pixel just above the water-occluded ray path and some 3 km beyond the geometric horizon tangent point, which suggests a height of $0.127 \times 23.5 / 2 + \sqrt{13 \times 3} \approx 7.5$ m. Ray bending calculations in the next section suggest a source height of 5 m above mean sea level.

On long paths or for levels of turbulence with RMS fluctuations $\sigma > 1.52$, observations summarized in the literature have shown that scintillation saturates. But for more moderate turbulence with $\sigma < 1.52$ a set of equations that can be used for modeling to match the June 26 observations is the Rytov solution:[14,15,16]

$$\sigma^2 \equiv \left\langle \left(\frac{I}{\langle I \rangle} - 1 \right)^2 \right\rangle = e^{4\sigma_\chi^2} - 1, \tag{5a}$$

where

$$\sigma_\chi^2 = 0.56 \left(\frac{2\pi}{\lambda}\right)^{7/6} \int_0^R ds \; C_n^2\{z(s)\} \; (s/R)^{5/6} \; ([R-s])^{5/6}. \tag{5b}$$

Here $\lambda \approx 3.92$ μm, s is the distance from the source and z(s) is the height dependence of C_n^2 along the path of length R. Note that for this scintillation of a spherical wave from a point source to a point sensor this weighting of C_n^2 along the viewing path is symmetric. This may seem counter to intuition based on the "shower-curtain" effect, but it is only for blurring and angular fluctuations that C_n^2 is weighted more toward the observer. Because C_n^2 is largest near the surface, the case for which turbulence inflicts the most degradation is for imaging from a periscope.[17] The assumption of lateral uniformity enters only when C_n^2 is calculated with the marine atmospheric boundary layer model.

---

[14]R.H. Hufnagel, *Propagation Through Atmospheric Turbulence*, Ch. 6 in The Infrared Handbook, revised edition, ed. W. L. Wolfe and G. J. Zissis, Infrared Information and Analysis Center, ERIM, 1985.

[15]R.R. Beland, *Propagation Through Atmospheric Optical Turbulence*, Ch. 2 in Atmospheric Propagation of Radiation, ed. F.G. Smith, Vol. 2 of The Infrared and Electro-Optical Systems Handbook, Executive Editors J. S. Accetta and D. L. Shumaker, Infrared Information and Analysis Center, ERIM, and SPIE Optical Engineering Press, 1993.

[16]S. Church, *IR Refraction and Scintillation for a Constant Flux Model of the Marine Surface Boundary Layer.*, Proc. IRIS Targets, Backgrounds and Discrimination., 1994

[17]F. Replogle, Jr. and C.W. Fairall, *Prediction of Optical Image Quality Near the Sea Surface from Meteorological Measurements*, TM No. 821008, 25 Jan 1982, Naval Underwater Systems Center, New London, CT.

IRTool is a workstation software package for calculating a variety of quantities for the maritime environment,[18] including index of refraction and C_n^2 as functions of height above the water. It is these values of C_n^2 that are used with the generalization of Equation (5) for finite sized source and aperture. Calculated results for the met conditions of June 26 with H_{source} = 5 m, H_{sensor} = 29.5 m and range = 23.5 km are summarized in Table 3. Low wind and higher, positive air-sea temperature difference both promote turbulence. The difference between measured and calculated turbulence appears to lie within the variability in the boat met data. The lower 0.4 °C air-sea temperature difference measured 10 minutes prior to the infrared image sequence gives a reasonable fit to the observed scintillation noted in Equation 4 of 48%.

Table 3: Calculated Scintillation for June 26, 1994

ASTD (3m)	V_{wind}(3m)	σ_{heater}	σ_{shroud}
+0.7 °C	1.6 m/s	152 %	121 %
+0.7 °C	3.0 m/s	132 %	94 %
+0.4 °C	1.8 m/s	69 %	55 %

The temporally uncorrelated nature of the observed scintillation at the 30 Hz frame rate agrees with modeling. For an eddy to significaltly contribute to scintillation it must be larger than the diffraction scale $\sqrt{(\lambda R)} \approx$ 0.28 m. Then since the main cross wind was due to helocopter drift that appeared in the imagry to be some 20 m/sec, the scintillation time constant sould be approximately 28 mSec as observed. (In independent measurements with a source on a boat the scintillations were observed to be faster than 1/60 sec.[19])

In addition to scintillation, the refractivity structure contributes to atmospheric blurring and random angular motion of the source. These quantities have also been evaluated numerically for the conditions of the June 26 observations. The calculated random angular motion is 8 μrad, which is small compared to the 127 μrad pixel IFOV and indicates that random motion should be small. The calculated atmospheric coherence length is 0.26 m, which is a bit larger than the 0.15 m aperture.

6.0 RAY BENDING AND THE APPARENT HORIZON POSITION

Infrared radiation does not travel along straight paths over the ocean. The 15-25 km distances to the horizon and beyond are long enough for refraction effects to become significant. Index of refraction is a function of height, and in the infrared this index of refraction N(z) depends mostly on air density[9] and hence on temperature and gravitational pressure with a weak humidity effect.

There are well established, but apparently imperfect, procedures for performing ray trace calculations through the refractive atmospheric medium. This is a three step process, first determining the index of refraction, N, temperature, T, etc. as a function of height, z, in the atmosphere; then applying Snell's law and, finally, picking out the demarcation ray with its declination angle to be defined as the water horizon. It is the first and last steps that still have some uncertainties in the lowest meter or so just above ocean waves. Details of these two issues are left to the Appendices. Simplified interpretations from the Monterey Bay field test are given in the next two subsections.

6.1 Occlusion by Surface Waves

Rays that skim close to the surface are likely to be blocked by a high water wave. This will be referred to here as surface occlusion. It limits the maximum detection range of distant, bright IR sources. A treatment of the statistics of occlusion by waves at the horizon is given in Appendix B. It is shown there and in Figure 9 that the transition height Δz from high $\approx$ 90% probability of ray passage to low $\approx$ 10% probability of ray passage at the horizon is about one standard deviation:

$$\Delta z_{\text{Probability Transition}} \approx 1\,\sigma, \qquad (7a)$$

---

[18] P. Davis, P., E. Branluund, S. Church, D. Klesch, E. Krumrey, and D. Crowder, *IRTool: An IRST X Windows Analysis Tool*, Proc. IRIS Targets, Backgrounds and Discrimination, 1994.

[19] Private communication from Robert Taylor of APL on results to be presented at the 1995 SPIE.

and that the skimming height z_{Pass} above mean sea level at which a ray is likely to pass non-occluded with 90% probability is

$$z_{90\%\ Pass} \approx 2.3\,\sigma \qquad (7b)$$

These values are represented in Figure 8 for June 30 when the wave height standard deviation was $\sigma \approx 0.5$ m, i.e., significant wave height had been estimated by the boat captain to be $H_{1/3} \approx 2$ m.

6.2 Land-to-Helicopter Data

Model ray trace plots for the meteorological conditions of June 26 and June 30 are presented in Figure 8. Source and helicopter sightings made with the staring infrared sensor are superimposed as data points that are either solid circles, open circles or crosses, but only for June 30 because accurate height information is missing for the 26th. Commensurate with the IR imagery reproduced in Figure 4, the solid circles denote that both the helicopter and the IR source were seen; the open circle neither. The X applies when only the helicopter was seen and the source below it was undetected. As can be seen in Figure 4 the 23.5 m distance between the helicopter exhaust and the IR source becomes, at 23 km range, an angular spacing of 8 pixels. At long range the lowest data points should become X's.

The model rays traced in Figure 8 are separated in angle at the sensor by half a pixel spacing, and their declination has been adjusted so that one of them dips at the to the height $z_{Pass} \approx 2.3\,\sigma$. Based on the reported wave heights for the 26th and 30th, these 90% passage rays are at $z_{Pass} \approx 0.2$-0.3 m and 0.5 m respectively. The dashed curves below this passage ray in Figure 10 show that for near neutral air temperatures the main thermal gradient up-bending or down-bending of rays is lost in the wave blockage region.

It is Figure 14 which gives the estimate that the scintillating IR source just above the passage ray must have been at approximately 5 m on June 26 during the 1155 image sequence represented in Figure 7.

The data points in Figure 9 are commensurate with the MBL ray bending model. The solid circles are all above the calculated 90% passage ray, and the open circle is below it.

One would like more extensive data confirmation. This would require several field test procedural modification such as: a lower sensor height and/or a conservative helicopter flight path so as to accomplish more hover time at the horizon, an integrating accelerometer as well as the laser altimeter on the helicopter for more accurate source height determination, more extensive and preferably buoy meteorology and oceanography, and better digital recording techniques for more and scintillation-averaged IR imagery. The Monterey Bay location has deep water with open-ocean like swells, but is dominated by diurnal sea-land, land-sea breezes with rapidly changing local met conditions, a short fetch and a mix of land aerosols.

6.3 The Land-to-Land Experiment

The height-scale bars on the right of Figure 8 suggest that it will be quite difficult to validate horizon wave occlusion in field tests looking out to an IR source carried on a moving platform such as a helicopter, drone or boat. The detection probability transition width for the waves at 7:00 pm on June 30 was estimated by of Eq. (7a) to be only half a meter. This is less then the apparent error in measuring the source height carried by the helicopter.

Wave occlusion and limiting-range ray bending tests can be much more precise when both the source and the sensor are on solid ground or on a fixed tower. Standard time-averaging GPS surveying can then give absolute heights to an accuracy of ±5 cm, and tide readings have similar or better accuracy. End points need to be at least a couple meters above mean sea level, and the location has to be chosen to represent the wave statistics of interest. Chesapeake Bay, for instance, being bounded and shallow has choppy waves with short swell. Monterey Bay has open-ocean like waves.

The path from Marina to Point Pinos was chosen for its convenient path length. With 12.8 km separation the source (a flash lamp) and sensor (a pair of binoculars) could both be moved up and down by simply walking to measured markers on the beach. Counting flashes seen in a given period gave a quantitative measure of wave occlusion probability, and varying end-point heights gave a scan of P(z). The measured results are presented in Figure 9.

In Figure 9 the solid circles are data points obtained from strobe flashes during a test when the significant wave height at the time of this test was 3.4 m. The heavy solid line is calculated as described in Appendix B. The general shape of the transition is well replicated with the calculated values shifted to the left of the measured values. The width of the transition from the 10% to 90% points is approximately 0.25 in normalized tangent height or 0.61 m in tangent height.

The calculated curves for P(z) in Figure 9 assume only straight ray paths. This is because, as shown in Figures 10 and 11, there appears to be an inconsistency when atmospheric effects and ray bending are included for the land-to-land experiments. One possible reason might be that there has been an error in the height measurements or in adjusting the zeros of measurements between the land survey and the tide data, but these numbers have been checked carefully. Survey heights were given relative to the National Geodetic Vertical Datum - 1929 (NGVD29). Mean tide level, the MTL is recorded at a NOAA tide level gauge located in Monterey relative to Mean Lower Low Water (MLLW), and the correction between these is that the NGVD29 level is 2.85 ft (0.87 m) above MLLW. Source and receiver heights were referenced to the (MLLW). The exact survey range was 12,808.83 m ±0.03 m.

Figure 10 exhibits the ray height as a function of surface range relative to MTL for source and receiver heights of 3.61 and 4.59 m. This ray corresponds to the circled data point in Figure 9 which was visible to the observer with unity probability. This observation conflicts with the analysis since there is no ray corresponding to ASTD's of -1.5 °C or -1.0 °C that connects the source to the receiver. To try to achieve a source-to-receiver connection with simple modeling, the ray tracing was repeated with heights measured relative to the wave troughs and the lower -1.0 C for ASTD. This zero-shifting device reduces model gradients above the water, but a ray could be made to connect only if it dipped well below the significant wave height. Good measurement and modeling of P(z) for the probability of passage of ray paths over horizon ocean waves will require more precise measurement of meteorology and geometry.

The field measurements offered ample opportunity to compare the horizon radiance profile with prediction.[20] The solid line in Figure 8 shows the measured vertical radiance profile taken on June 30 at 6:50 pm PDT. The measured profile corresponds to a four pixel average. Positive look-down angles correspond to views above the horizon. The solid circles above the horizon are the radiance values calculated by Lowtran and the solid circles below the horizon are the mean radiance values calculated with the statistical sea surface radiance model which expresses the radiance as a function of the wave slope. Note that the measured radiance profile exhibits little radiance clutter. This is attributed to the proximity of the mean wave slope to the null in the radiance function.

7.0 OCEAN RADIANCE PROFILES

The field measurements offered ample opportunity to compare the horizon radiance profile with prediction.[21] The solid line in Figure 8 shows the measured vertical radiance profile taken on June 30 at 6:50 pm PDT. The measured profile corresponds to a four pixel average. Positive look-down angles correspond to views above the horizon. The solid circles above the horizon are the radiance values calculated by Lowtran and the solid circles below the horizon are the mean radiance values calculated with the statistical sea surface radiance model which expresses the radiance as a function of the wave slope. Note that the measured radiance profile exhibits little radiance clutter. This is attributed to the proximity of the mean wave slope to the null in the radiance function.

8.0 CONCLUSIONS

The results reported here are part of a continuing series of measurements in the IRAMMP program for characterizing the near-horizon infrared scene around ships and the behavior, characteristics and detectability of small infrared sources just above or just below the ocean horizon. As listed in Table 4, five quantities were

---

[20]M.D. Mermelstein, *Midwave and Longwave Infrared Radiance and Clutter at the Ocean-Sky Horizon*, Vol. 19, No. 18, Optics Letters, Sept. 15, 1994.

[21]M.D. Mermelstein, *Midwave and Longwave Infrared Radiance and Clutter at the Ocean-Sky Horizon*, Vol. 19, No. 18, Optics Letters, Sept. 15, 1994.

measured on this field test. Controlled simulation of a dim, low, distant missile was achieved with a heated IR source carried by helicopter.

TABLE 4. SUMMARY OF THE FIVE KINDS OF MEASUREMENTS. Small IR or visible source at > 20 km range and/or viewed at < 1 mRad above or below the ocean horizon.

Field Measurement	Phenomenon Involved	*Analysis Methods* & Software Tools	Modeling Success	Remaining Issues
IR Source Radiance During Range "Fly-Out" to Horizon	Molecular Absorption Aerosol Extinction Aerosol Solar Scattering	Lowtran	Moderate	Coastal Met Data Scintillation Drop Out Shroud Radiance
Scintillation of Distant, Low IR Source	Marine Boundary Layer C_N^2 Path Weighting	*M.O. Marine Bndry Layer* *C_N^2 formulas* IR Tool	Moderate	Coastal Met Data Correlation Time
Birds, Their Radiance & Detection	Same as for IR Source + Solar Reflecting Source	Lowtran	Good	(Could Refine)
Ray Occultation by Horizon Waves of Low Viewing Paths	N(z) from MBL Ray Bending Wave Cutoff Statistics	*Ray Trace Codes* *Formulas* IR Tool	Poor	Precision Measurements
Wave Radiance and Clutter in IR Horizon Scenes	Same as for IR Source + Wave Slope Statistics Wave Shadowing Horizon Geometry	*NRL Statistical Code* Lowtran IR Tool	Good	Coastal Met Data Lowtran Inputs

The measured radiance of an IR source at long range over the water decreases essentially as expected due of atmospheric transmission loss. But scintillation becomes significant at long ranges on low paths, so dim sources can be discerned only part of the time. This should pose difficulties for software acquisition and tracking of slewing targets. Dependence of intensity on height in very low-altitude aerosols was not measurable and is not expected. Solar position and the scattering of its radiation from dense sea-wind aerosols changed during the course of an hour long helicopter flight test. This changed background radiance but not source contrast radiance or detectability.

Lowtran was used to calculate both the infrared sky background including solar scattering and the atmospheric attenuation loss with dense sea aerosols for this IR source "fly-out." As noted in the table, the agreement between modeling and measurement on this test was only moderately good. The main unsatisfactory feature was not that Lowtran is limited to a laterally uniform meteorological environment, but that the available meteorological measurements were insufficient for characterizing the environment. Input parameters for Lowtran had to be treated as variable fitting parameters rather than known quantities.

The main lessons learned from the IR source "fly-out" tests are that our abilities to simulate an IR source and to model atmospheric losses and scintillation are reasonable, but that characterization of near-coastal environments is difficult. Winds may change daily or in tens of minutes in speed or in direction to or from land, and this effects changes in air temperatures, aerosol type and density and thereby dispersive ray bending, atmospheric losses and solar scattering.

Birds were observed out to 6 km, and their signatures were confirmed to be from solar reflection. At this range they will be problematic clutter for IRST's.

The cut off of low, skimming rays by waves depends on wave height and wind speed. Modeling of the probability of occlusion by waves predicts that detection ranges of sea skimmers should vary by ≈2 km from sea state 2 to 4. Precision measurement and model verification of occlusion by waves is needed. Also, the conventional understanding of the optical structure of the lowest meter or two of the marine boundary layer may not be in agreement with experiment, and will require further research.

Detailed wave-slope and shadowing statistical modeling of ocean-surface infrared radiance and clutter are in good agreement with values measured in this and previous experiments.

APPENDIX A: EFFECTS OF OCEAN SURFACE ROUGHNESS IN MBL

There are at least four coded forms of the marine atmospheric boundary layer (MBL) model for the atmospheric index of refraction N(z) as a function of height z for the infrared. They give comparable numerical results and are all based on the Monin-Obuhkov stability scaling. Refinements in the codes include gravity gradient effects from the non-flat earth, empirical parameters and linking of differential equations for temperature, humidity and wind speed.

Monin-Obuhkov stability scaling is based on an understanding of the nature of turbulent flow over a roughened but otherwise extended, flat surface. See Figure A1 for a sketch of turbulence over water waves. The basic assumptions are: 1) that there exists a scale mixing length ξ proportional to turbulence size ρ for changes in all the meteorological parameters wind speed, temperature and humidity, 2) that average turbulence size $\rho(z)$ at a given height must be short near the surface, large far away, and in fact that $\xi(z) = kz$, with $k \approx 0.4$, and 3) that there must be stability in mean velocity, temperature and humidity as functions of height, i.e., that momentum, heat and humidity transfer between layers of thickness $\xi(z) = kz$ must be the same for all layers. To translate this to equation form note that conductivity varies inversely with turbulence size $\rho(z)$, and that gradients of wind speed, temperature and humidity all vary inversely with conductivity and hence inversely with ρ and z. Then for any of the height-dependent meteorological parameters u(z), $\Delta u \propto 1/\xi = 1/kz$, or

$$\frac{\partial u(z)}{\partial z} = \frac{u^*}{\xi(z)} = \frac{u^*}{kz}. \tag{A1}$$

The wind speed, temperature and humidity each have different gradient proportionality parameters, but with u(z) the wind speed profile, u* is called the friction velocity. It is the gradient of index of refraction that enters into Snell's law and ray tracing, but in general the directly measurable quantities are the integral of Eq. (A1)

$$u(z) = \frac{u^*}{k} \ln \frac{z}{z_o}, \tag{A2}$$

The integration constant z_o is taken to be a roughness parameter characteristic of the surface the air is passing across and so is independent of meteorological conditions or the meteorological variable being considered. Once z_o is determined, the gradient proportionality constants u*, etc. are determined in field tests by making measurements of temperature, wind speed and humidity at a fixed test height, about 3 m on the met boat used during the June, '94 tests at Monterey. It is indirectly through this matching of u(z) to a measured value that the roughness parameter effects gradients as for index of refraction and thence ray bending.

The surface roughness is not a measure of wave height. Rather, it is fixed empirically by making measurements of temperature, wind speed or humidity as functions of height above the surface, doing a recursive fit versus ln(z) and extrapolating downward. So z_o is taken from the zero on a semi-log plot. There is variability in the values thus determined, and it is not clear that there is no dependence on sea state, but typically in open seas measurements reported in the literature have given approximately

$$z_o \approx 0.3 \text{ mm}. \tag{A3}$$

This very small roughness parameter does not mean that there were no waves during the measurements. The z_o is an integration constant, and the use of Eqs. (A1) and (A2) in the troughs of waves may be at variance with the underlying concept of the existence of an average turbulence size ρ and a transport scale length ξ at each height z.

Wave peaks will certainly terminate the passage of infrared or visible rays, and a statistical analysis for setting a reasonable cutoff height is presented in Appendix B. But a separate, not yet satisfactorily resolved issue showed up in the brief land-to-land measurements made during the June, '94 field test at Monterey Bay. Calculated ray traces seem to bend too strongly upward when they pass just above the wave crests in the "cool" air 1.5 °C colder than the water at 9-10 pm on June 30.

The modeling used in Appendix B assumes straight line ray paths. With upbending, MBL calculations of ray paths could not be made to connect between the measured heights of the source and observer. Measurements of ASTD or of heights might be in error, but these have been checked carefully, especially the adjustment of zeros used in tide versus land survey measurements. It is possible that when subjected to carefully controlled testing the true gradients in index of refraction just above the wave crests are not as severe as that implied by Eq. (A1).

This Appendix B is a review of how changes might best be made in the marine atmospheric model at very low heights. In keeping with similarity scaling this is a search for how reasonably to reduce the average turbulence size $\rho(z)$ and hence scale mixing length $\xi(z)$ at heights z just above the wave crests.

The simplest approach computationally and perhaps conceptually would be to shift the zero for the z axis downward to a position below mean sea level. This shift, perhaps with a minor adjustment in z_o, could be treated as a new parameter to be adjusted until model ray path connection is achieved between source and receiver. This would change modeled values of temperature, etc. at higher altitudes.

Perhaps more satisfying but computationally more difficult is to mitigate the low-altitude 1/z dependence of the mixing scale length with an equation like

$$\xi(z) = \xi_o \left[\frac{z^{*2}}{z^2 + z^{*2}}\right] + kz \left[\frac{z^2}{z^2 + z^{*2}}\right] \rightarrow \begin{cases} \xi_o ; & z < z^{*2} \\ kz ; & z > z^{*2} \end{cases}$$

A rational for this, sketched in Figure A1, is that a good part of the turbulence looping back behind wave crests is much larger than the simple 1/z dependence of $\xi(z)$ would imply. Part of this larger-scale turbulence must lift into a region just above the wave crests, and a demarcation for this uplifting has been sketched in Figure A1 at the height z*. There must be all sizes of turbulence in this region, but the important sizes that contribute to upward transport of heat, humidity and momentum transfer are the larger ones. Conductivity is proportional to turbulence size.

Integration of Eq. (A2) with this new scaling length and matching boundary conditions at height h yields the following gradient and velocity profiles:

$$\frac{\partial u(z)}{\partial z} = \left[\frac{u_h}{g_1(h) + g_2(h)}\right] \frac{1}{\xi(z)} \qquad \text{and} \qquad u(z) = u_{10} \left\{\frac{g_1(z) + g_2(z)}{g_1(h) + g_2(h)}\right\} \tag{A4}$$

where

$$g_1(z) = \frac{1}{3} \ln\left[\frac{z^3 + b^3}{z_o^3 + b^3}\right], \qquad b^3 = \xi_o z^{*2}$$

$$g_2(z) = \frac{1}{3b^3} \ln\left[\frac{z + b}{z + z_o}\right] - \frac{1}{6b^3} \ln\left[\frac{z^2 - bz + b^2}{z_o^2 - bz + b^2}\right] + \frac{1}{\sqrt{3}b^2} \left\{ \tan^{-1}\left[\frac{2z - b}{\sqrt{3}b}\right] - \tan^{-1}\left[\frac{z_o - b}{\sqrt{3}b}\right] \right\}.$$

Eqs. (A4) are plotted in Figures A2a and A2b for h = 10 m with the label "hybrid" for comparison with the usual similarity scaling (Eq. (A2)) labeled "log." The values used for ξ_o and z* were 5 cm and 3 m respectively.

An alternative possibility once proposed for treating the effect of waves was to assume that sinusoidal swell locally raises and lowers the 1/z dependence of meteorological gradients, i.e., that $dN(z)/dz \propto 1/z_{local} = 1/[z+(H/2)\cos(x)]$ should be averaged over lateral position. Since turbulence size and height are inversely related, this is exactly the opposite to the rational suggested above, and can be expected to increase rather than decrease gradients just above the wave crests. And numerically a singularity in effective scale length can be seen to occur at the wave crest because of the contribution 1/[z-(H/2)] in the x average, $\partial u/\partial z = (1/2\pi) \int dx / z_{local}$. Performing the x average over a period 2π, integrating in z and matching boundary conditions u_h for u(z) at height h yields the following gradient and velocity profiles:

$$\frac{\partial u(z)}{\partial z} = \frac{u_h}{\left[\dfrac{h + \sqrt{100 - (H/2)^2}}{H/2}\right]} \frac{1 + \dfrac{z}{\sqrt{z^2 - (H/2)^2}}}{z + \sqrt{z^2 - (H/2)^2}}, \qquad u(z) = u_h \left\{ \frac{\ln\left[\dfrac{z + \sqrt{z^2 - (H/2)^2}}{H/2}\right]}{\ln\left[\dfrac{h + \sqrt{h^2 - (H/2)^2}}{H/2}\right]} \right\}. \tag{A6}$$

APPENDIX B OCCLUSION BY OCEAN WAVES

Rays that skim close to the surface are likely to be blocked by a high water wave. This will be referred to here as surface occlusion. It limits the maximum detection range of distant, bright IR sources.

The "tangent point," or range position of lowest ascent of a ray path, is surrounded by a "tangent region" along which the ray remains close to the surface. The location of this tangent point and length of the surrounding tangent region will depend on details of ray bending induced by air-sea temperature difference and other meteorological conditions, but a typical tangent region is one to two kilometers long. It contains hundreds of statistically independent subregions where a candidate wave peak could protrude upward and be the first rogue that terminates the ray path in question. These independent subregions will be labeled starting from the tangent point with the index i = 0, ±1, ±2, ... The probability that a wave could have height z above mean sea level in the i^{th} subregion is a normal distribution $\phi(z+z_i)$ where the z_i are spacings between mean sea level and the ray in question displaced downward to be truly tangent to mean sea level at the tangent point where $z_0 = 0$.

What is needed is the probability P(z) that a ray will pass by the surface without being terminated by any wave in any of the subregions. The normal and integrated probability distributions in any one subregion are

$$\phi(z+z_i) = \frac{1}{\sqrt{2\pi}\sigma} e^{\frac{-(z+z_i)^2}{2\sigma^2}} \quad \text{and} \quad \Phi_i(z) = \int_{-\infty}^{z} dz' \, \phi(z'+z_i), \tag{B1a}$$

$\Phi_i(z)$ is the probability of passage over the i^{th} subergion. The probability of ray passage over the entire path is thus

$$P(z) = \prod_{i=0\,\pm1\,\pm2\ldots} \Phi_i(z) \approx \Phi_0^N(z) = \left[\int_{-\infty}^{z} dz' \, \phi(z') \right]^N, \tag{B1b}$$

where N is to be set as an estimate of the number of active subregions in the tangent region.

The plot of Eq. (B1b) in Figure B1 shows that results depend only weakly on N for N > 10. A reasonable value based on the curvature of the earth is somewhere in the range of 300.

To use the more accurate Eq. (B1b) one needs the spacings z_i between sea level and the downward displaced ray path. For a straight path over the earth with radius R_e the distance to the i^{th} subregion, if each is of size λ_s, is $i\lambda_s = \sqrt{(2Rz_i)}$, so the z_i would be

$$z_i = \frac{(i\lambda_s)^2}{2R_e}. \tag{B2}$$

If, further, the spacing between statistically independent wave regions is assumed to be the swell length in fully developed open seas, the zi can be scaled with wind speed u_{10} measured at 10 meters via

$$\lambda_S = (2\pi/g)(1.2\, u_{10}^2), \qquad H_{1/3} = 4.0\,\sigma, \text{ or } H_{1/3} = 0.0292\, u_{10}^2. \tag{B3}$$

Figure B1 suggests that the transition height Δz from high ≈ 90% probability of ray passage to low ≈ 10% probability of ray passage is about one standard deviation:

$$\Delta z_{\text{Probability Transition}} \approx 1\,\sigma \tag{B4a}$$

The skimming heights z_{Pass} above mean sea level at which a ray is likely to pass non-occluded with P ≈ 90% and z_{Cutoff} for P ≈50% are

$$z_{Pass} \approx 2.3\,\sigma, \quad z_{Cutoff} \approx 1.8\,\sigma \tag{B4b}$$

An example of the dependence of detection range on wind-speed induce wave obscuration is given in Figure B2. Shown is the time lag in time between when a missile should first appears over the horizon with 50% probability of ray passage through the waves and the time it would first appear if the sea surface were perfectly smooth. The missile is assumed to be flying at Mach 1 and altitude of 5 m while the sensor is positioned at a height of 30 m. Changing sea state can significantly alter the engagement time line. According to the model an increase of sea state from 2 to 4 introduces a 3 second delay.

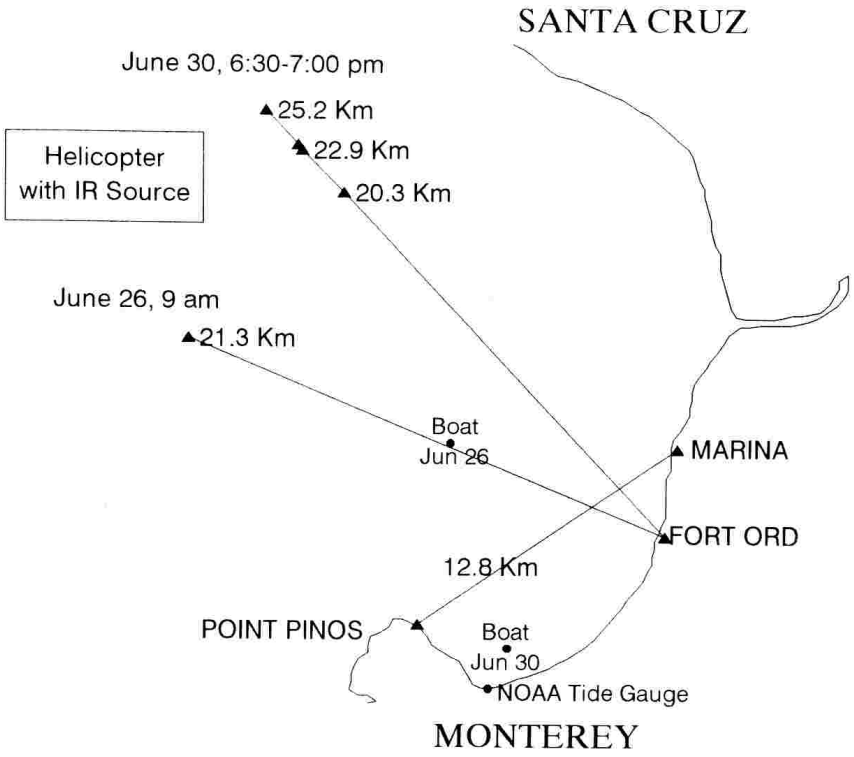

FIGURE 1 FIELD TEST VIEWING PATHS ACROSS MONTEREY BAY. A helicopter and IR source were viewed with a staring 3.75-4.11 μm sensor looking in northwesterly directions out to the horizon. A flashlamp was viewed in the visible with binoculars along the 12.8 km path from Marina to Point Pinos.

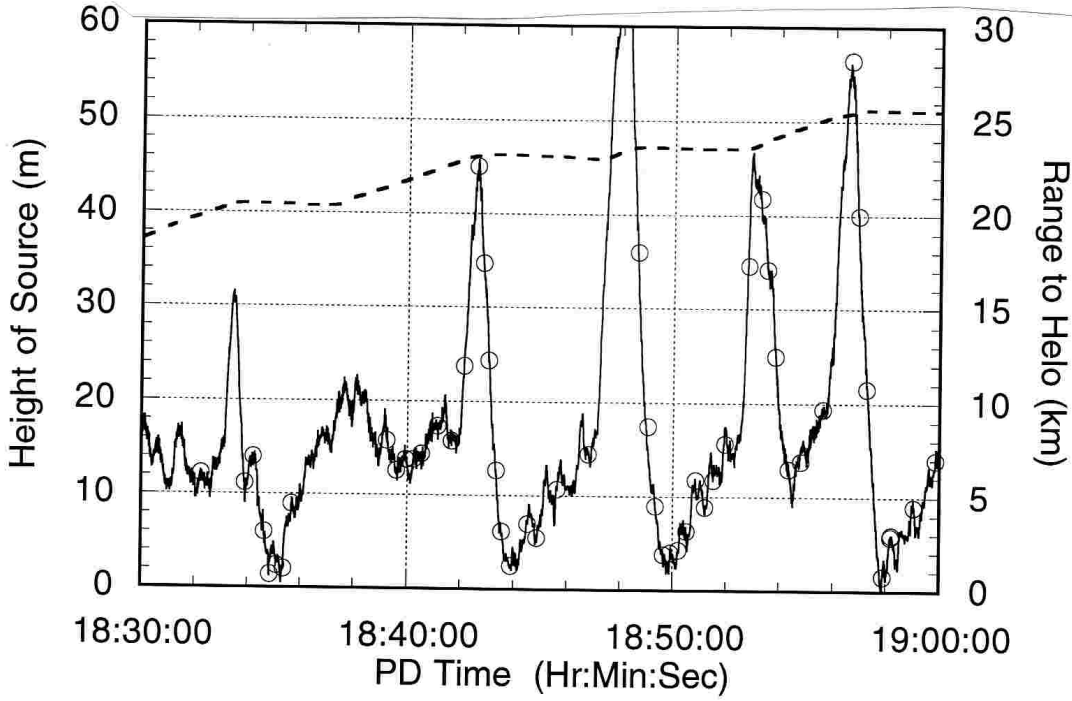

FIGURE 2 IR SOURCE HEIGHT AND RANGE ON JUNE 30. Source height, the solid curve, was determined by a laser altimeter on the helicopter. Wave motion is evident and limits height determination accuracy to about 1 m. The circles denote the times when digital staring-array IR imagery was recorded such as shown in Figure 4. Source range, the dashed curve, was derived from differential GPS.

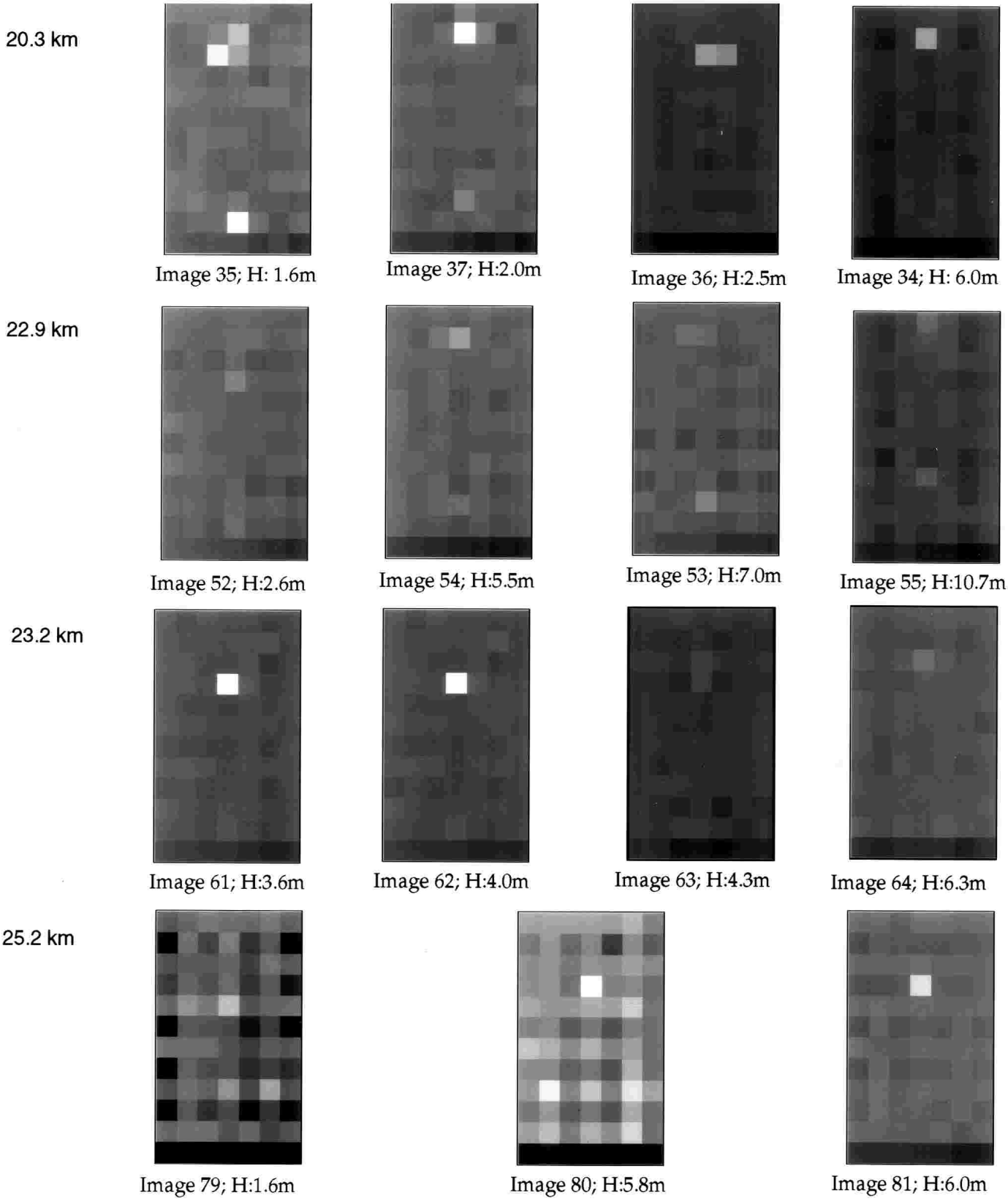

FIGURE 4 IR SOURCE AND HELICOPTER JUST ABOVE THE HORIZON. Radiance contrast signature of the source in these scenes is plotted and modeled in Figure 6, and height-range is plotted with ray trace modeling in Figure 8. Scintillation of both the IR source and the helicopter exhaust is apparent, but the source appears to have sometimes disappeared below the horizon. The ≈ 23.5 m spacing between helicopter exhaust and IR source subtends 7 to 8 of the 127 μRad sensor pixels at the ranges indicated. Sensor spatial NEI is 3 to 6 x 10^{-16} W/cm^2, and sensor height is 29.5 m. The air temperature was neutral, generally 0.1 °C colder than the water but 0.1 °C warmer at the time of the longest range. The lowest row of pixels in these images sometimes splits and is sometimes below the horizon.

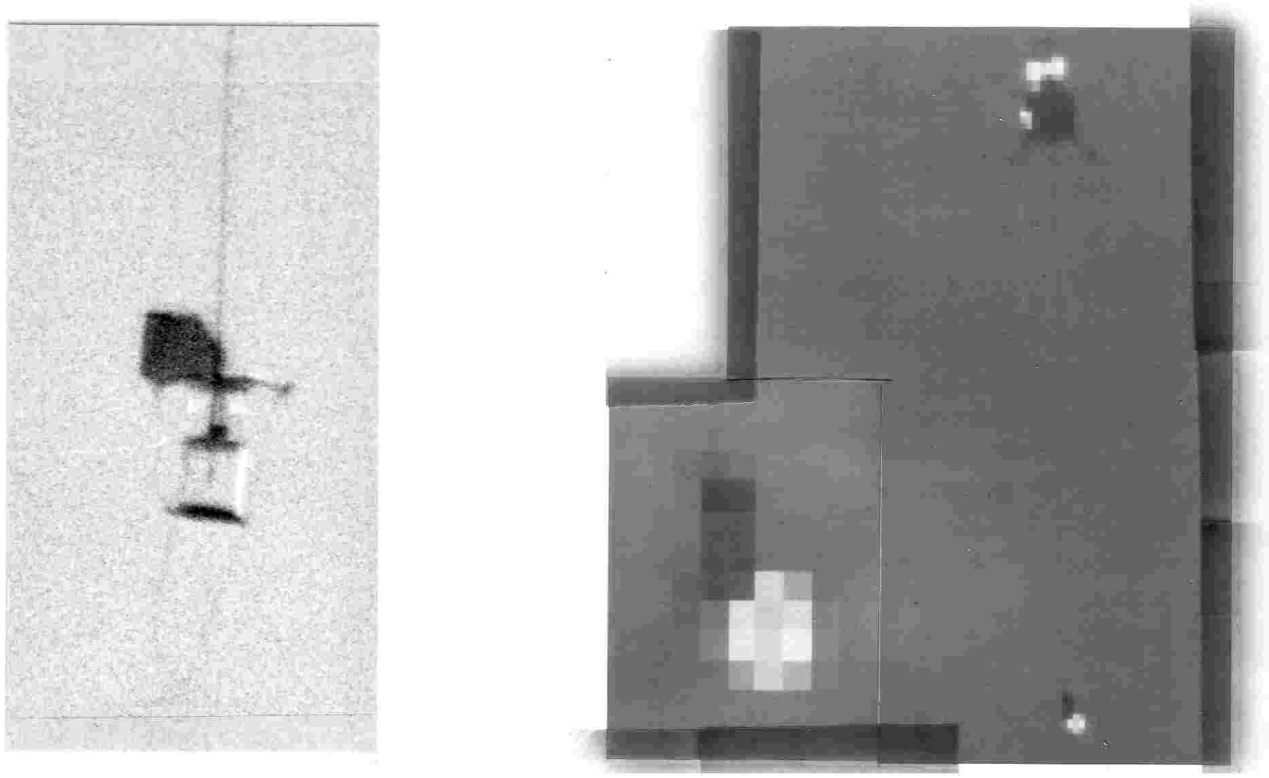

FIGURE 3 IR SOURCE CARRIED BY HELICOPTER. The enlarged visible image of the IR source (left) shows some of its detail. It consists of a small, 13 cm x 3.3 cm, 868 watt electric heater inside a transparent 49 cm x 41 cm polythene wind shroud. The enlarged IR image of the IR source (inset, right) shows that just after the heater is turned off there appears to be infrared emissions from the wire mesh supporting the shroud.

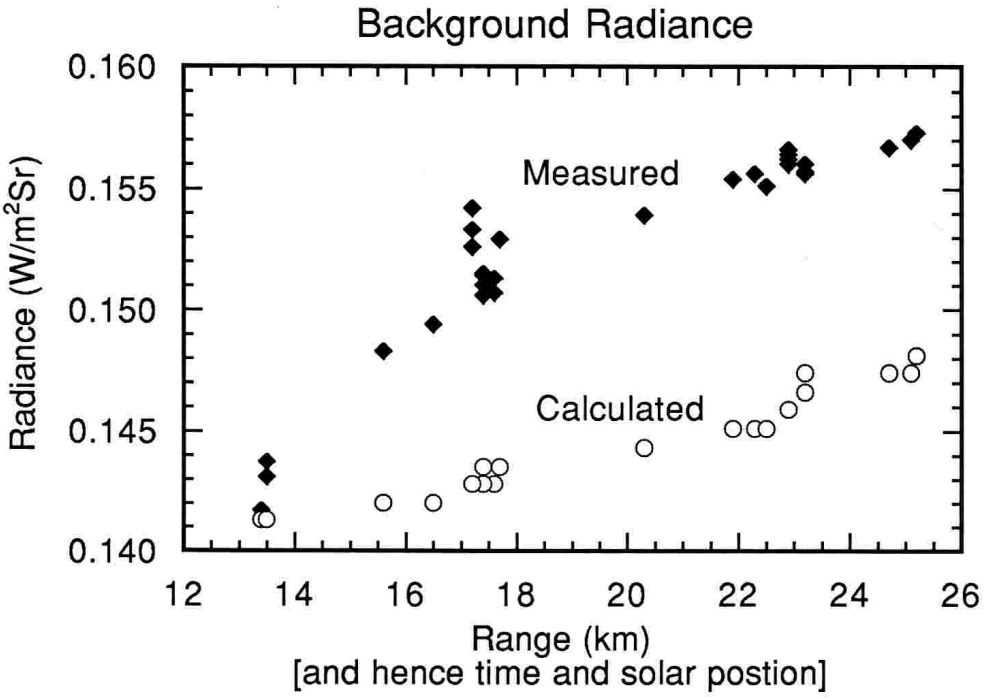

FIGURE 5 BACKGROUND RADIANCE VERSUS TIME ON JUNE 30. The correspondence between time and range during this helicopter flight is given in Figure 2. The sun was moving nearer to the sensor's line of sight, this inducing more forward scattering off dense aerosol mist over the ocean. Diamonds are measured values as taken from scenes like those in Figure 4. Circles are Lowtran calculations including solar scattering and a user-input atmosphere.

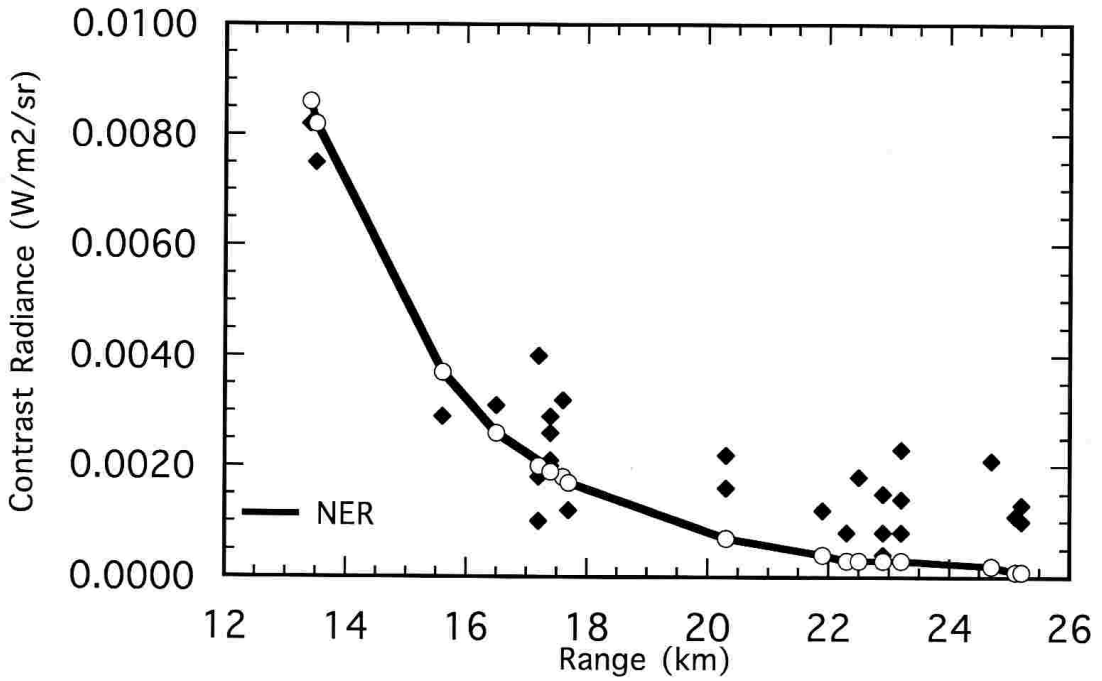

FIGURE 6 SOURCE CONTRAST VERSUS RANGE ON JUNE 30. Diamonds are measured values of the IR source when it is seen as taken from images like those in Figure 4. Scintillation scatter is on the order of ± 50 %. The flatness of this data plot is probably due to scintillation dropout to below the sensor's spatial noise of NER = 0.0012 W/m^2Sr. Circles are Lowtran calculations , again including solar scattering and user-input atmosphere.

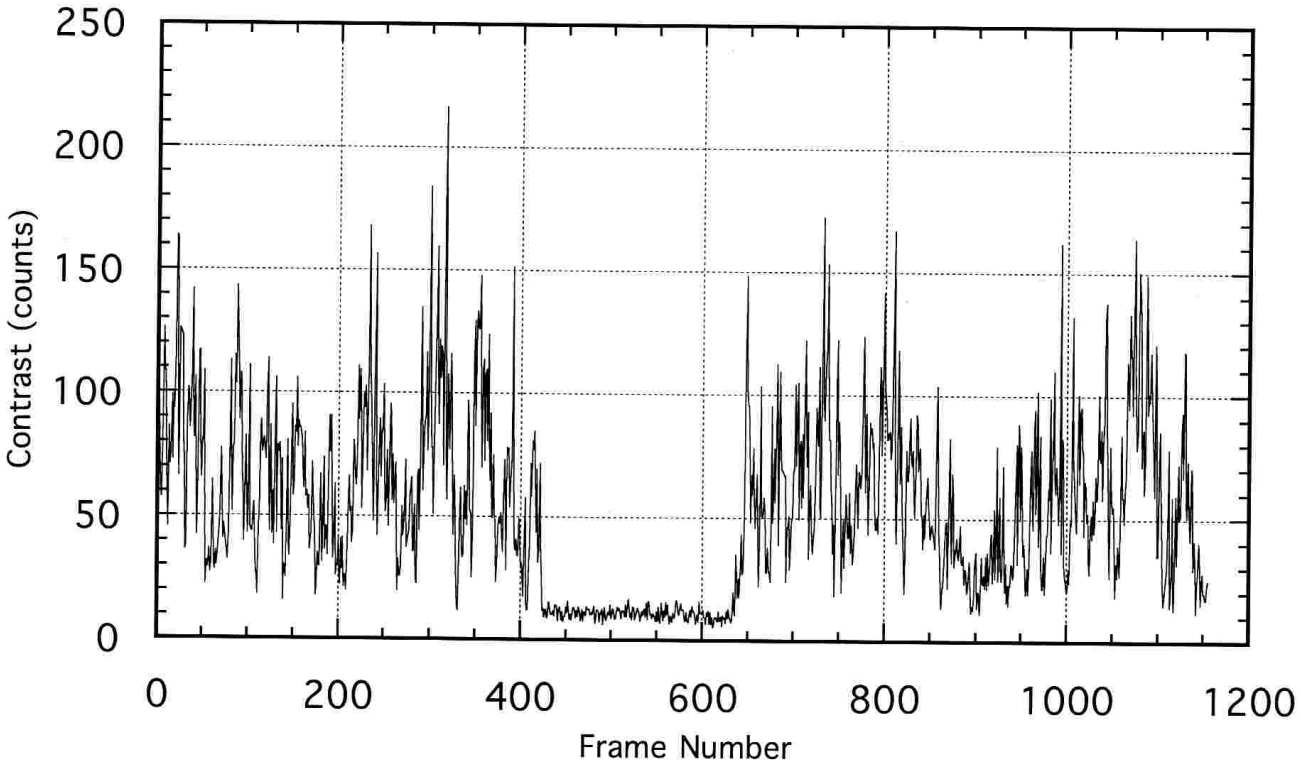

FIGURE 7 RADIANCE SCINTILLATION OF IR SOURCE AT 23.2 KM ON JUNE 28. The source is being carried by a helicopter that is attempting to hover but drops during the middle of this 28 sec sequence by the equivalent of one sensor pixel, this momentarily placing the source below the ocean horizon. In the pixel just above the horizon the mean normalized scintillation was measured to be 48 %. Modeling is complicated by rapidly changing of meteorological conditions as noted in Table 2.

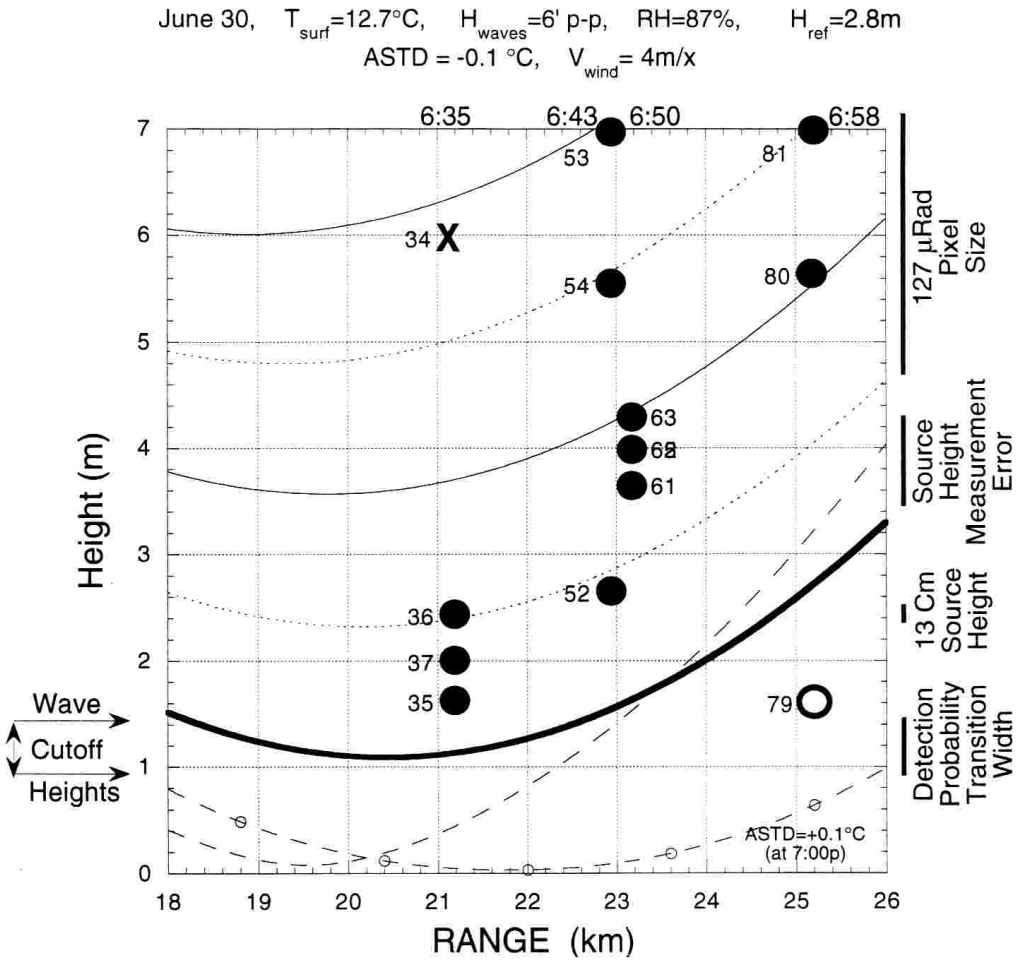

FIGURE 8 HEIGHT-RANGE DATA OF IMAGES IN FIGURE 4. A solid circle means that both the source and helicopter appear in Figure 4; the X indicates disappearance of the source and open circle that neither can be seen. The bold ray trace dips to the level where it should have a 90 % probability of passing the wave peaks, so the model water horizon is just below this ray. Sources at heights above this are seen in Figure 4, the one below is not.

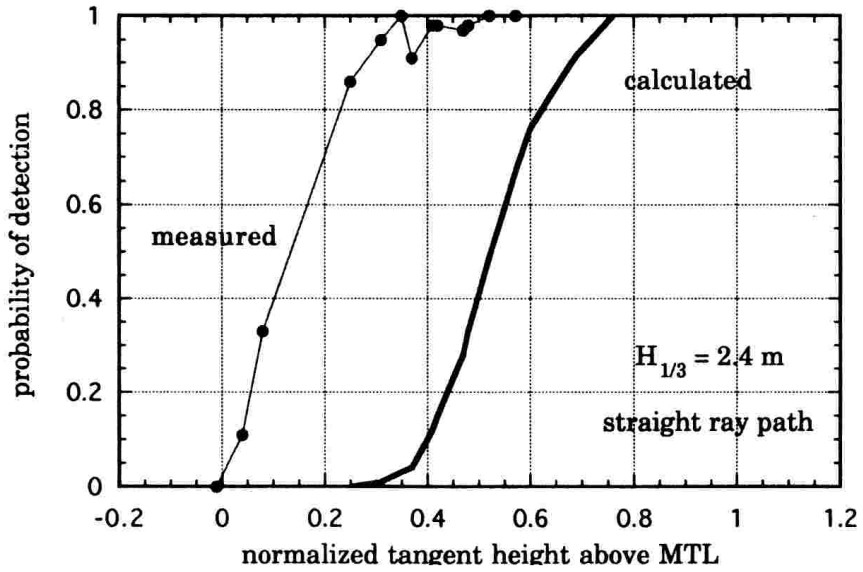

FIGURE 9 SEEING PROBABILITY AS PATH SKIMS WAVES IN LAND-TO-LAND TEST. Probability of ray passage decreases as path height drops. The measured and calculated curves agree in shape but are shifted in height. Height is given in units of significant wave height.

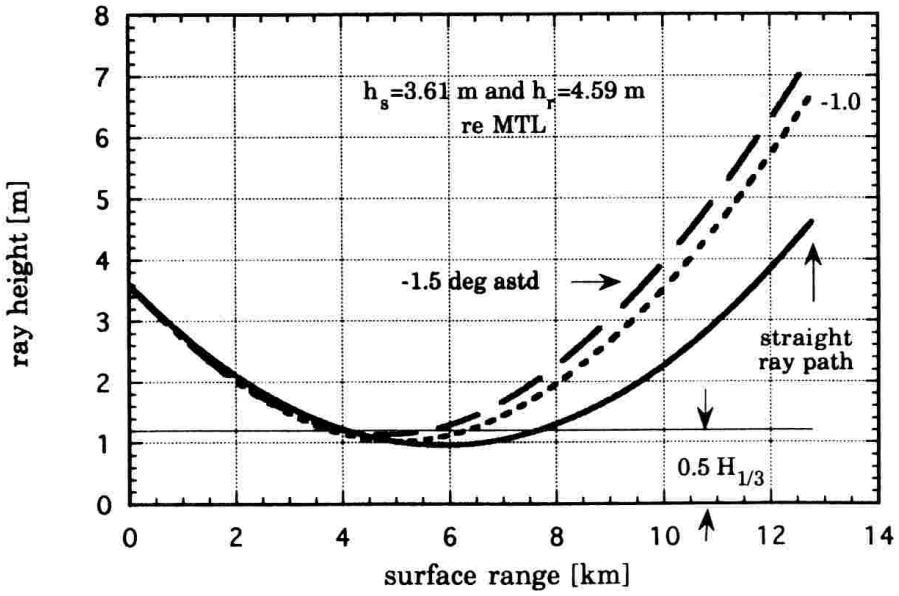

FIGURE 10 LAND-TO-LAND RAY TRACING WITH STANDARD MBL. The measured air-sea temperature difference was -1.5 °C, but ray traces with this and a lower ASTD could not be made to connect source and observer because of upbending from strong index of refraction gradients just above the wave crests.

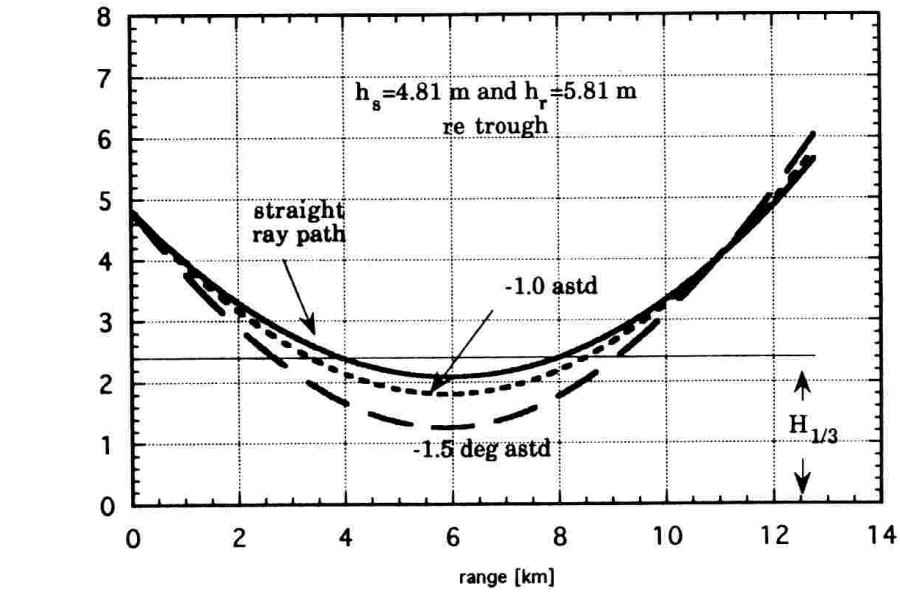

FIGURE 11 LAND-TO-LAND RAY TRACING WITH REDUCED GRADIENTS. Low-elevation index gradients were reduced compared to the standard marine boundary layer values used in Figure 10 by shifting the zero of height downward one meter. Model ray traces could still not be made to connect source and observer because of still too strong upbending.

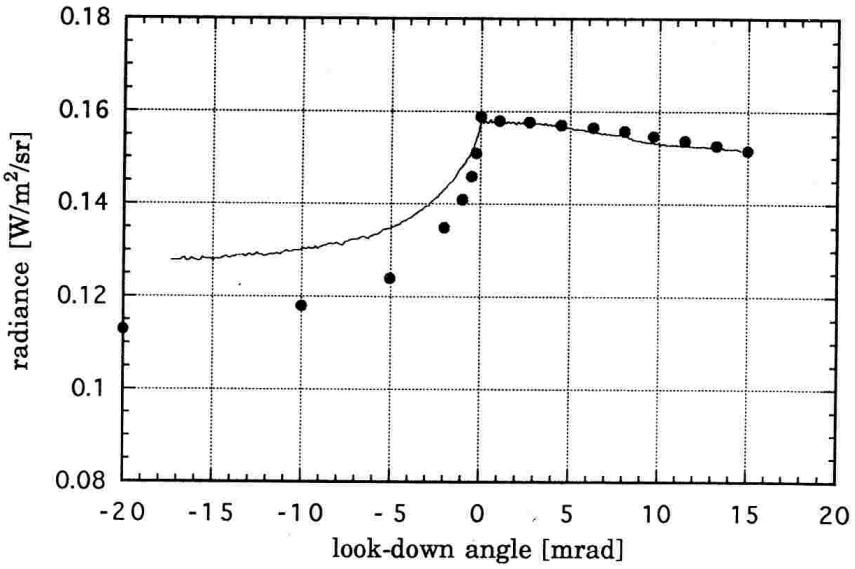

FIGURE 12 VERTICAL RADIANCE PROFILE OF HORIZON. Data is given by the solid line, calculations by the series of dots. The time of day was just before 7 pm when the sun gave strong forward scattering off the dense aerosols above the ocean. The inputs to use for Lowtran are a significant problem for modeling both above and below the horizon. Wave statistics, wave shadowing, horizon geometry and reflection versus emission have all been included in the treatment of the water surface. Ocean clutter variations in radiance are low because of details of wave slope statistics for the prevailing wind.

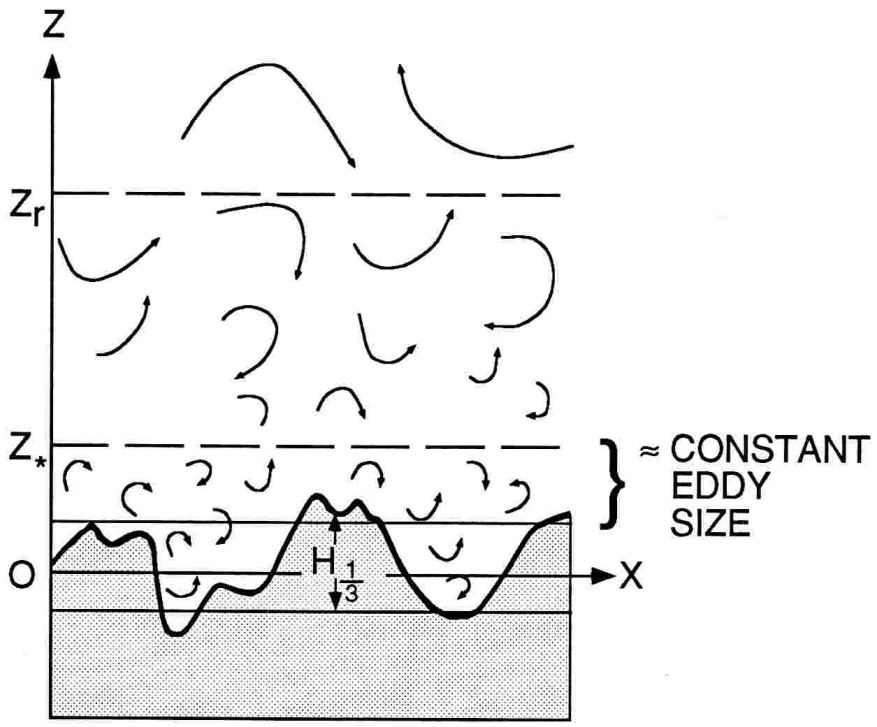

FIGURE A1 TURBULENCE SCALES JUST ABOVE WAVE CRESTS. The size decrease of turbulence over nominally flat surfaces normally trends down in proportion to height, but in the mixing region in and just above ocean waves may depart from this rule. Wave-induced, wave-sized swirls probably lift up slightly above the wave crests. The larger sizes of turbulence are dominant for upward transport of heat, momentum and humidity, so for modeling purposes a height z* is used to denote a region of effectively constant turbulence size. The turbulence size proportional to height relationship is assumed not to hold below z*.

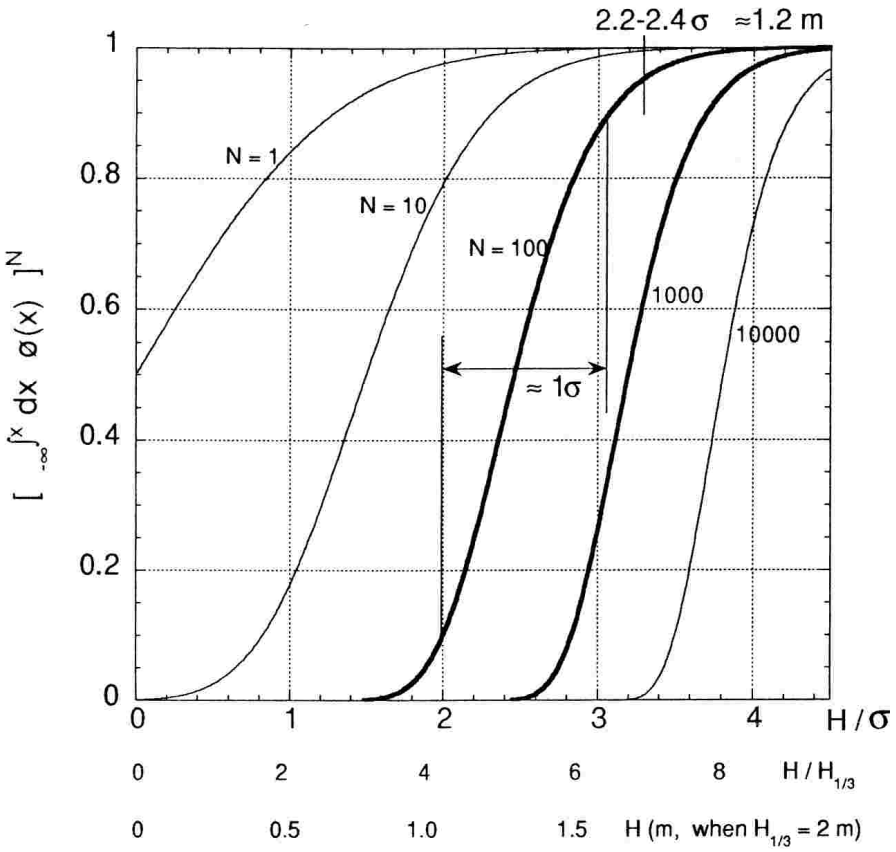

FIGURE B1 APPROXIMATE SEEING PROBABILITY THROUGH WAVE OCCLUSION. Powers, N, of the integral to height z of the normal probability distribution are plotted as a function of z and N. For N > 10 the dependence on N is mild. At N > 100 the 90 % point is near 2.3 s and the transition width from 90 % to 10% is about one s.

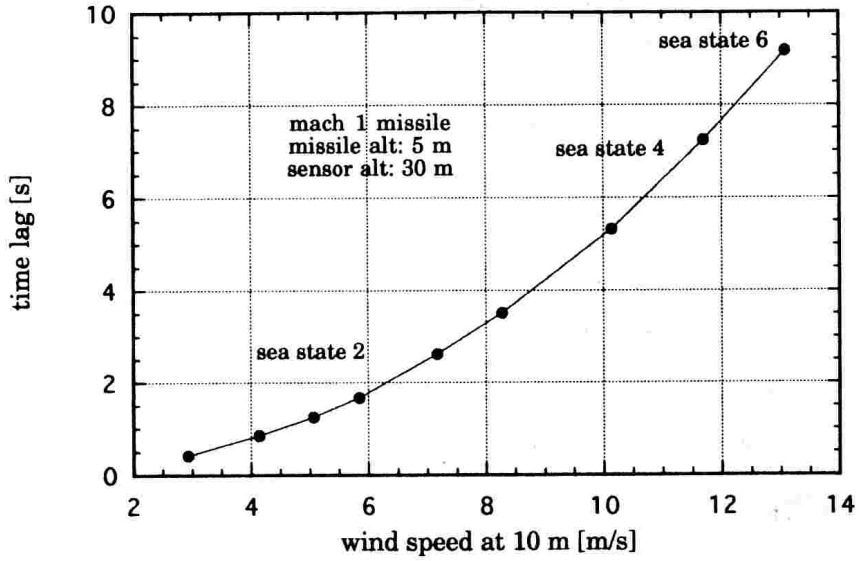

FIGURE B2 MISSILE DETECTION TIME LAG DUE TO WAVE OCCLUSION.